Available online at www.sciencedirect.com
ScienceDirect
Trans. Nonferrous Met. Soc. China 35(2025) 902−920
Transactions of Nonferrous Metals Society of China
www.tnmsc.cn

Improving mechanical properties of extrusion additive manufacturing WC−9Co cemented carbide via green warm isostatic pressing

Cai CHEN[1], Run-xing ZHOU[1], Zu-ming LIU[1], Yong-xia LI[1,2], Dan ZOU[2], Yi-ming CHANG[2], Xu-lin CHENG[2]

1. State Key Laboratory of Powder Metallurgy, Central South University, Changsha 410083, China;
2. Hunan Boyun Dongfang Powder Metallurgy Co., Ltd., Changsha 410205, China

Received 26 October 2024; accepted 7 February 2025

Abstract: To tackle the common issue of green defects in material extrusion (MEX) additive manufacturing (AM) cemented carbides, warm isostatic pressing (WIP) was introduced to eliminate defects of MEX WC−9Co cemented carbide greens, thereby improving both microstructure uniformity and mechanical properties of sintered bodies. The results indicate that WIP reduces defects in MEX greens, thus decreasing the dimensions and numbers of defects, modifying shapes of pores within sintered bodies, while preserving surface quality and shape characteristics. Compared with WC−9Co prepared via MEX followed by debinding and sintering (DS), the hardness of WC−9Co prepared using MEX−WIP−DS does not change significantly, ranging HV_{30} 1494−1508, the transverse rupture strength increases by up to 49.3%, reaching 2998−3514 MPa, and the fracture toughness remains high, ranging 14.8−17.0 MPa·$m^{1/2}$. The mechanical properties surpass comparable cemented carbides fabricated through other AM methods and are comparable to those produced by powder metallurgy. The integration of green WIP into MEX−DS broadens the MEX processing window, and improves the overall mechanical properties of MEX AM WC−Co cemented carbides.

Key words: material extrusion additive manufacturing; WC−Co cemented carbide; warm isostatic pressing; defect; microstructure; mechanical properties

1 Introduction

WC−Co cemented carbide, as the most widely used type of cemented carbide, is tailor-fabricated according to its tasks by powder metallurgy and has wide applications in aerospace, resource extraction, equipment manufacturing, electronic information, etc. The reliance on dies in powder metallurgy restricts the production of complex-shaped cemented carbide parts, but additive manufacturing (AM) offers a promising solution to overcome this limitation [1,2].

Currently, many studies have reported on the AM of WC−Co cemented carbides [3−5]. However, powder bed fusion (PBF) WC−Co cemented carbide faces persistent issues such as difficult-to-eliminate pores, cracks, abnormal grain growth, and various brittle multi-phases due to oxidation and decarburization [6−9]. By employing AM equipment to prepare greens and then subjecting them to debinding and sintering (DS), the material extrusion (MEX)−DS technology could eliminate pores, cracks, and deleterious phases that occur in PBF WC−Co cemented carbides, and produce high-performance cemented carbide products with microstructures similar to those produced via powder metallurgy [10−12]. For instance, ZHAO et al [13−15] have fabricated WC−8Co cemented carbide with a relative density of 99.3%, a hardness of HV_{30} 1323, and a transverse rupture strength of 1861 MPa by optimizing the binder composition,

Corresponding author: Zu-ming LIU, Tel: +86-13975809336, E-mail: lzm@csu.edu.cn
DOI: https://doi.org/10.1016/S1003-6326(24)66722-1

increasing the filler ratio, and reducing the printing-layer thickness of MEX. Similarly, KIM et al [16] used MEX−DS to prepare WC−10Co cemented carbide with a relative density of 99%, a hardness of 16.5 GPa, and a fracture toughness of 10.1 MPa·m$^{1/2}$, respectively. CHEN et al [17] have utilized the MEX−DS process to prepare WC−9Co cemented carbide with a relative density of 99.7%, a hardness of HV_{30} 1525, a transverse rupture strength of 3492 MPa, a fracture toughness of 20.4 MPa·m$^{1/2}$, respectively. However, the MEX process is likely to cause wedge-shaped stacked pores and interlayer bonding defects within the greens, which deteriorate the uniformity of the sintered microstructure and negatively affect the overall mechanical properties. Although altering the microfilament overlap ratio and printing-layer thickness can mitigate these issues of MEX greens [17], increasing the microfilament overlap ratio reduces surface quality and mechanical properties, while decreasing the printing-layer thickness can multiply the preparation time of MEX cemented carbide greens. Moreover, these strategies are often constrained by the performance of the feedstock and the limitations of the MEX production system. Therefore, minimizing the defects of MEX greens while maintaining their shape characteristics is crucial for the industrial application of MEX−DS WC−Co cemented carbides.

Warm isostatic pressing (WIP) is a densification process that uses high-pressure gas and offers the advantage of independently controlling temperature and pressure. This enables the mitigation of stacked pores and interlayer bonding defects in MEX-prepared greens and is beneficial for reducing sintered defects in WC−Co cemented carbides produced through MEX−DS while fully preserving their shape characteristics. Therefore, we propose the integration of applying WIP on green into the MEX AM technology for the first time to reduce the defects in MEX cemented carbide greens and improve the uniformity of the sintered microstructure, thereby improving the overall mechanical properties of the sintered samples derived from defective greens. This approach facilitates the highly-efficient preparation of cemented carbide products with mechanical properties comparable to those of powder metallurgy counterparts. The results hold significant potential for advancing the industrial application of AM technologies for cemented carbides.

2 Experimental

2.1 Processing

The process flowchart from feedstock to final sintered sample is shown in Fig. 1. The MEX feedstock, with 54 vol.% powder loading, was prepared using a wax-based organic binder and WC−9Co composite powder, following the same processes as reported in our previous work [17]. To analyze the impact of the green WIP process on the defects and microstructure of MEX cemented carbide greens, three types of MEX greens were prepared for WIP using a MEX machine (UP−250, Shenzhen Sublimation 3D Technol Co., Ltd., China) with the same MEX parameters as green samples 1, 3, and 9 in our previous work [17]. The fixed MEX parameters included a nozzle diameter of 0.4 mm, a printing speed of 30 mm/s, a printing temperature of 150 °C, a feedstock extrusion flow rate of 60%, an interlayer angle of microfilament deposition channel of [45°, −45°], and a build platform

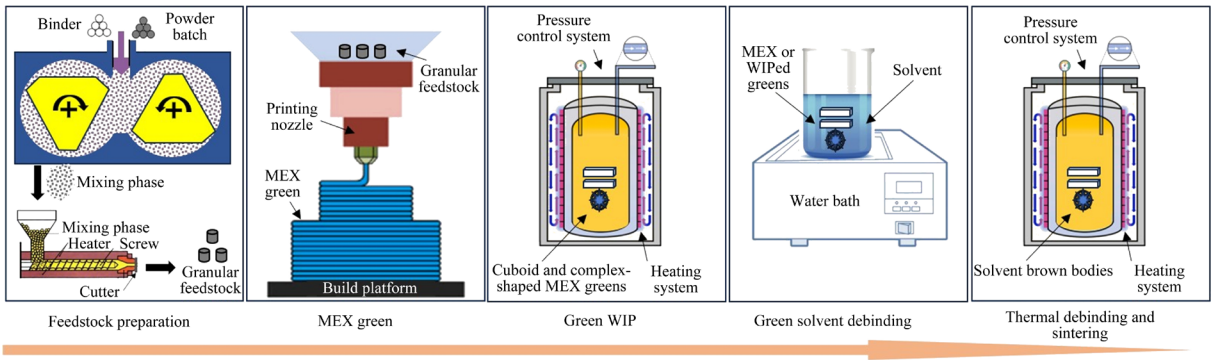

Fig. 1 Process chain flowchart of feedstock preparation, MEX green, green WIP, green solvent debinding, as well as thermal debinding and sintering

temperature of 100 °C. The variable MEX parameters and their corresponding MEX green codes are listed in Table 1.

The WIP-treated (WIPed) samples, according to Table 2, were obtained by subjecting MEX green samples M_1, M_3, and M_9 to WIP treatment using a WIP machine (SIP30×30/120−1600−10). The WIP temperatures and pressures were designed based on the TG−DSC curves of the binder in our previous work [17]. The WIP process was conducted in an argon gas with a holding pressure time of 10 min.

Table 1 MEX greens and variable MEX parameters [17]

MEX green	Microfilament overlap ratio/%	Printing-layer thickness/mm
M_1	30	0.1
M_3	0	0.1
M_9	0	0.3

Table 2 WIPed sample codes and WIP parameters

WIPed sample code	MEX green sample for WIP	WIP temperature/ °C	WIP pressure/ MPa
$T_{60}P_1M_1$	M_1	60	1
$T_{60}P_1M_3$	M_3	60	1
$T_{60}P_1M_9$	M_9	60	1
$T_{60}P_5M_1$	M_1	60	5
$T_{60}P_5M_3$	M_3	60	5
$T_{60}P_5M_9$	M_9	60	5
$T_{120}P_1M_1$	M_1	120	1
$T_{120}P_1M_3$	M_3	120	1
$T_{120}P_1M_9$	M_9	120	1
$T_{120}P_5M_1$	M_1	120	5
$T_{120}P_5M_3$	M_3	120	5
$T_{120}P_5M_9$	M_9	120	5

The sintered WC−9Co cemented carbide samples were prepared through solvent debinding and continuous thermal debinding−vacuum-pressure sintering of the MEX and WIPed green samples. Solvent debinding involved n-heptane extraction debinding at 30 °C for 12 h and kerosene extraction debinding at 30 °C for 1 h. The continuous thermal debinding−vacuum-pressure sintering process was carried out using the same machine, with the process parameters set accordingly as those in our previous work [17].

The sintered samples prepared by directly debinding and sintering the MEX green samples were named MEX-DS samples, with their codes corresponding to those of the respective MEX green samples. Correspondingly, the sintered samples prepared by debinding and sintering the WIPed green samples were named MEX-WIP-DS samples, with their codes matching those of corresponding WIPed green samples.

2.2 Characterization

The microstructures of green and sintered samples were characterized using a scanning electron microscope (SEM, Quanta FEG 250). The distribution of elements in sintered samples was analyzed by energy-dispersive X-ray spectroscopy (EDS) using an SEM (Quanta FEG 250). Electron backscattered diffraction (EBSD) data and grain sizes were collected using a NordlysMax2 (Oxford) probe configured on the SEM (TESCAN MIRA4 LMH). The surface roughness was measured using a 3D optical profilometer (WYKONT9100). Internal structures of sintered samples with a size of approximately 1 mm × 1 mm × 1 mm were analyzed using a microfocus computed tomography scanner (micro-CT, Dondo d2).

The relative densities of green and sintered samples were the ratios of the actual densities to theoretical densities and could be calculated by Eq. (1):

$$d = \frac{\rho}{\rho_0} \times 100\% \tag{1}$$

where d is the relative densities of green or sintered samples, ρ and ρ_0 represent the actual density and theoretical density of samples, respectively. The actual densities were measured using the Archimedes drainage method, and the theoretical densities were calculated based on the mass fractions and theoretical densities of the various constituents of the powder batch and binders.

The hardness was determined using an automatic turret digital Vickers hardness tester (Suzhou Qiantong Instrument Equipment Co., Ltd., China). The transverse rupture strength (R_{bm}) was evaluated using a universal testing machine (Instron 3369) with type B specimens ((5.25±0.25) mm × (6.5±0.25) mm × (20±1) mm) according to ISO 3327: 2009, and a loading rate of

1 mm/min was applied. The fracture toughness (K_{IC}) was calculated according to ISO28079: 2009 using an automatic turret digital Vickers hardness tester (Suzhou Qiantong Instrument Equipment Co., Ltd., China). Each mechanical property test of the sintered body was carried out three times, and the results were obtained as the average values.

3 Results and discussion

3.1 Impact of WIP on microstructure and properties of MEX greens

3.1.1 Green defects and their evolution

Figure 2 illustrates SEM images for the defects and microstructure of the MEX and WIPed WC−9Co cemented carbide greens. During the MEX process of WC−Co cemented carbide greens, the feedstock is melted and extruded through a heated nozzle to form extruded microfilaments. These extruded microfilaments and the previously deposited ones go through four stages−surface contact, neck growth, molecular diffusion, and cooling to form a bonding interface. The MEX green shape is primarily maintained by the backbone binders (the insoluble backbone component of the binder). Consequently, in the MEX green M_9 with a larger printing-layer thickness, a large number of wedge-shaped (or triangular) stacked pores are formed due to the neck growth at the bonding interface between the deposited microfilaments. Additionally, due to deposition pressure and surface tension, the residual stress caused by rapid cooling, curing, and shrinkage of extruded microfilaments leads to the formation of interlayer bonding defects. Reducing the printing-layer thickness and increasing the microfilament overlap ratio can alter the angle between adjacent deposited micro-filaments and the morphology of the neck at the bonding interface, resulting in a significant reduction of stacked pores in the green samples M_1 and M_3.

Green WIP exerts a crucial influence on the defects and their evolution in MEX greens. The microstructure changes in the WIPed greens are closely related to the WIP temperature and pressure. As depicted in Fig. 2, when the WIP pressure is set to be 5 MPa, the areas of the stacked pores in WIPed greens are conspicuously reduced, and exhibit a flat shape. However, a considerable number of interlayer cracks are present in the three samples of $T_{120}P_5M_1$, $T_{120}P_5M_3$, and $T_{120}P_5M_9$. When the WIP pressure is reduced to 1 MPa, no visible pores and interlayer bonding defects are observed in the WIPed samples $T_{120}P_1M_1$ and $T_{120}P_1M_3$. The area of the stacked pores in the WIPed sample $T_{120}P_1M_9$ is also significantly reduced compared with its MEX state, and a limited number of interlayer bonding defects are observed upon cross-section. These defects may be associated with the deformation of the binder

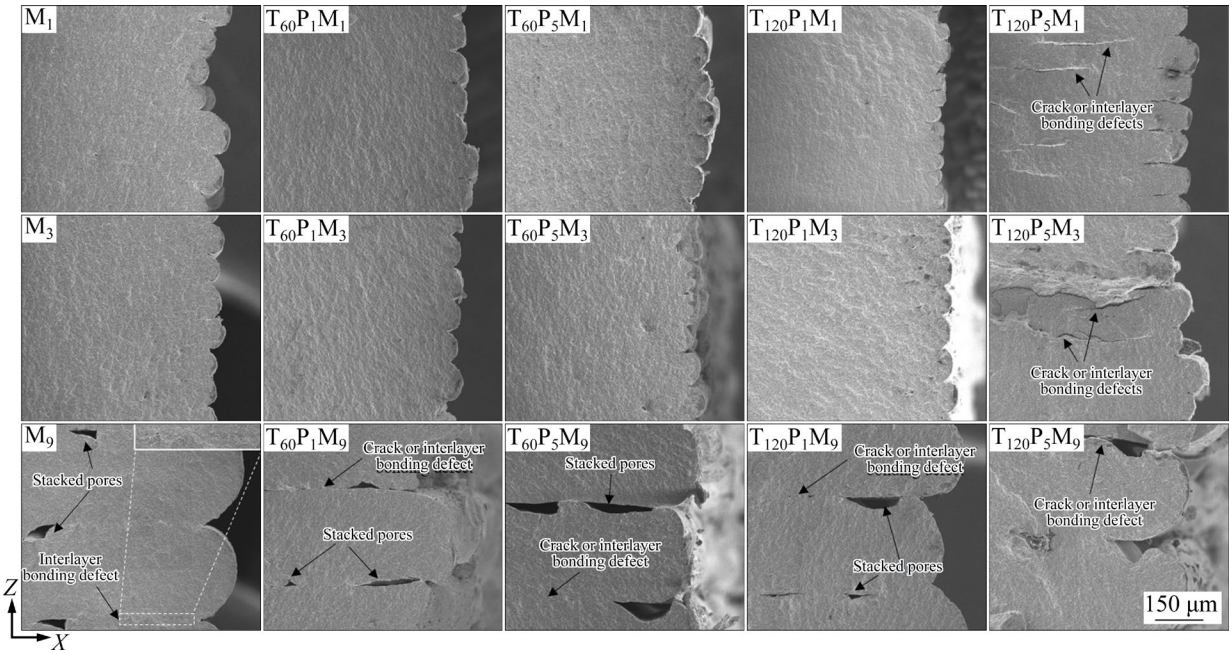

Fig. 2 SEM images for defects and microstructure of MEX and WIPed greens

during WIP. When the WIP temperature is decreased to 60 °C, no visible pores and interlayer bonding defects are detectable in the samples $T_{60}P_1M_1$ and $T_{60}P_1M_3$ WIPed with the pressure of 1 MPa. However, a small number of interlayer bonding defects are still present in $T_{60}P_1M_9$, which may be attributed to the flattening of some pore defects that may not have been completely healed under the WIP pressure. Overall, the elevated temperature causes the melting or softening of the partial backbone binder, resulting in non-uniform deformation of the green under substantial WIP pressure. By appropriately lowering the WIP temperature and pressure, only low-molecular plastic binder (plasticizing component of binder) melts, while the strength of the backbone binder that maintains the green shape remains high comparatively. As a result, the stacked pores in the MEX cemented carbide greens can contract or heal during green WIP.

3.1.2 Relative density and transverse rupture strength of greens

(1) Relative density of greens

Figure 3 illustrates the relative densities and transverse rupture strength of MEX and WIPed green samples. The relative density is closely associated with the defects in the MEX green samples. Specifically, the relative densities of samples M_1, M_3, and M_9 are measured as 98.45%, 97.84%, and 97.14%, respectively. WIP has a significant influence on the relative densities of the greens, as shown in Fig. 3(a). By WIP with the pressure of 5 MPa, the relative densities of all WIPed samples decrease compared with their MEX states, likely due to excessive pressure introducing new defects into the green samples. Conversely, by WIP with the pressure of 1 MPa and temperature of 60 °C, the relative densities of WIPed green samples demonstrate the most significant increase. In particular, the relative density of $T_{60}P_1M_1$ increases by 0.15% compared with that of M_1, reaching approximately 98.60%, while the relative density of $T_{60}P_1M_9$ increases by 0.54% compared with that of M_9, resulting in relative density of approximately 97.68%. The results indicate that the optimal WIP parameters are temperature of 60 °C and pressure of 1 MPa, significantly increasing the relative density of MEX green samples with a large number of defects and low relative density.

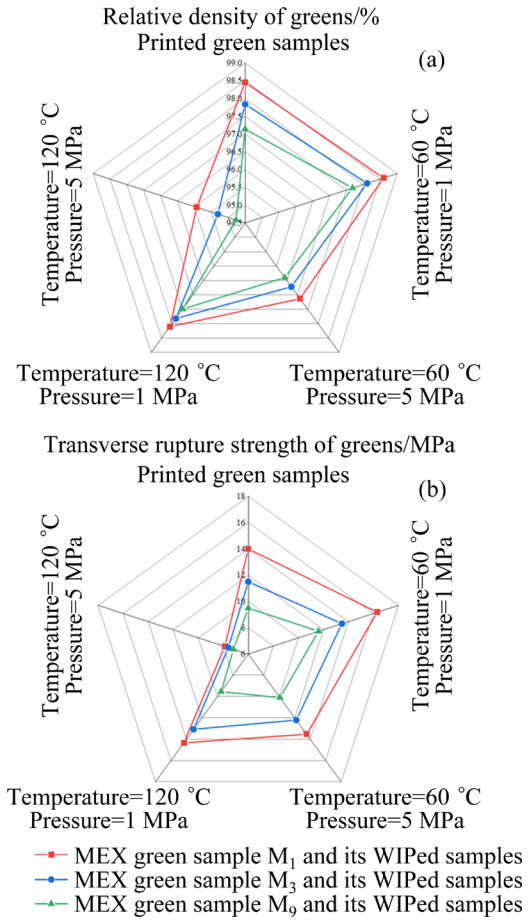

Fig. 3 Relative densities and transverse rupture strength of MEX and WIPed green samples: (a) Relative density; (b) Transverse rupture strength

During the WIP of MEX cemented carbide greens, the heated molten plastic binder flows and diffuses under pressure, resulting in the displacement and rearrangement of small-sized powder particles, thereby altering their contiguity states. Concurrently, the backbone binder experiences deformation and polymer chain flow [18]. The WIP densification process essentially involves the filling or compressing of certain pores within MEX green and forming denser bonds at interlayer or intralayer interfaces (Figs. 4(a, b)), primarily driven by the displacement and rearrangement of small-sized powder particles caused by the flow of plastic binder and the plastic deformation of backbone binder. The impact of particle displacement and binder plastic deformation on WIP densification varies with different temperatures and pressures [19]. At relatively high WIP temperatures and pressures, there is a reduction in green strength due to the melting or softening of some backbone binders, and

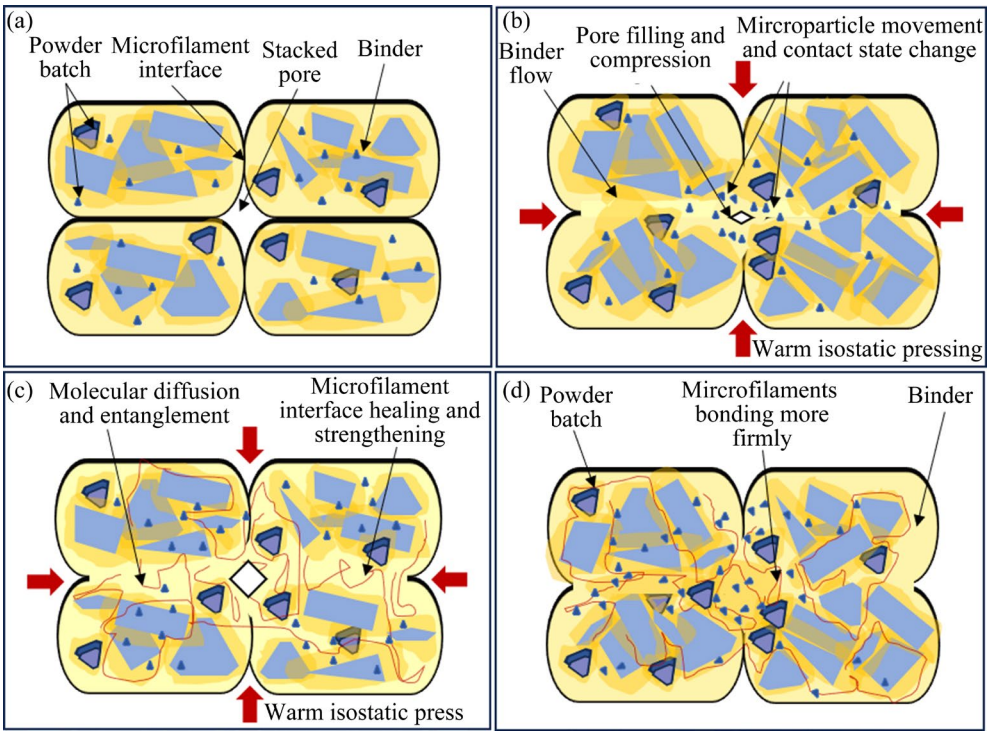

Fig. 4 Defects of MEX WC−Co cemented carbide green and evolution of pores and interfaces during WIP process: (a) Defects in MEX green; (b) Pores compression; (c) Microfilament interface strengthening; (d) Green densification and strengthening

non-uniform deformation may occur within the green when subjected to high pressure, potentially leading to new cracks and other defects that adversely affect the WIP densification. By employing an appropriate WIP temperature and pressure (60 °C and 1 MPa, respectively), the backbone binders can maintain a high strength, which is beneficial for the greens to achieve pores compressing and filling while preserving their shape characteristics. As a result, this approach significantly increases the relative densities of greens (Fig. 4(d)).

(2) Transverse rupture strength of greens

Figure 3(b) illustrates the transverse rupture strength of MEX and WIPed green samples. The transverse rupture strength of these WIPed samples is closely linked to their microstructure and is influenced by both the WIP temperature and pressure. After WIP with a pressure of 1 MPa, the transverse rupture strengths for the WIPed samples $T_{60}P_1M_1$ and $T_{120}P_1M_1$ are measured as 16.31 and 14.34 MPa, respectively, representing increases of 16.50% and 2.43% compared with that of MEX green sample M_1 (14.00 MPa). In contrast, the WIPed samples $T_{60}P_1M_9$ and $T_{120}P_1M_9$ have strengths of 11.61 and 9.52 MPa, respectively, which correspond to increases of 22.21% and only 0.21% over that of green sample M_9 (9.50 MPa). Increasing WIP pressure to 5 MPa, there is a notable reduction in transverse rupture strength for all the WIPed samples, and $T_{120}P_5M_1$, $T_{120}P_5M_3$, and $T_{120}P_5M_9$ exhibit the values decreasing to 7.88, 7.60, and 7.18 MPa, respectively. This decline can be attributed to an increase in temperature causing the plastic binder within the MEX green sample to melt and the backbone binder to soften, consequently leading to non-uniform deformation under high WIP pressure, which results in the new defects. Although the relative density of the green sample $T_{120}P_1M_9$ increases significantly after WIP, flattened pores can still be observed. These pores may act as fracture sources, thereby causing the transverse rupture strength to exhibit a limited improvement. These results indicate that an increase in relative density typically corresponds to an increase in transverse rupture strength, but the relationship between relative density and transverse rupture strength of MEX greens is not necessarily linear.

The green strength has an important influence on its debinding defects and shape retention ability.

For sinter-based AM, it determines the feasibility of producing high-precision and complex thin-walled structures [20]. The strength of MEX cemented carbide green is closely related to the neck growth of interface, molecular diffusion, and cooling shrinkage processes of deposited microfilaments [18,21]. To further enhance the strength of MEX greens, it is essential to adopt optimal parameters such as reducing printing-layer thickness, increasing microfilament overlap ratios, and improving filling densities. These strategies could alter the morphology of neck growth at the interfaces between deposited microfilaments, thereby reducing the stacked pores and interlayer bonding defects in the MEX greens [22,23]. However, these measures also may significantly increase the preparation time for MEX greens and compromise the surface quality. During the green WIP process, the temperature is maintained for an extended period above the glass transition temperature or the melting point of the thermoplastic binder. The WIP pressure can increase the contact area between deposited microfilaments, promoting polymer chain flow and molecular entanglement of binder, thereby facilitating the increase of bonding strength of the deposited microfilament interfaces (Figs. 4(c, d)). In summary, the green WIP process facilitates the diffusion of binder molecules at the interfaces between deposited microfilaments, enhancing the bonding strength at the deposited microfilament interfaces and ultimately facilitating the increase of the strength of MEX cemented carbide greens.

3.2 Impact of WIP on sintered defects and microstructure

3.2.1 Sintered defects

(1) Sintering shrinkage and shape retention

A dense structure represents a fundamental requirement for cemented carbide to achieve satisfactory mechanical properties [24]. To investigate the influence of WIP on the sintered microstructure and mechanical properties of MEX−DS WC−9Co cemented carbides, three WIPed green samples with significantly improved performance ($T_{60}P_1M_1$, $T_{60}P_1M_3$, and $T_{60}P_1M_9$) were selected for debinding and sintering. Figure 5 illustrates the sintered shrinkage rate and surface roughness of WC−9Co cemented carbide samples using the MEX−WIP−DS process. Figure 5(a) shows that the shrinkage rate is closely related to the relative density of WIPed green samples. Compared with the WC−9Co cemented carbide prepared by MEX−DS [17], the shrinkage rates of sintered samples $T_{60}P_1M_1$ and $T_{60}P_1M_3$ slightly increase, while the shrinkage rate of sintered sample $T_{60}P_1M_9$ significantly increases and also exhibits anisotropic characteristics. Specifically, the

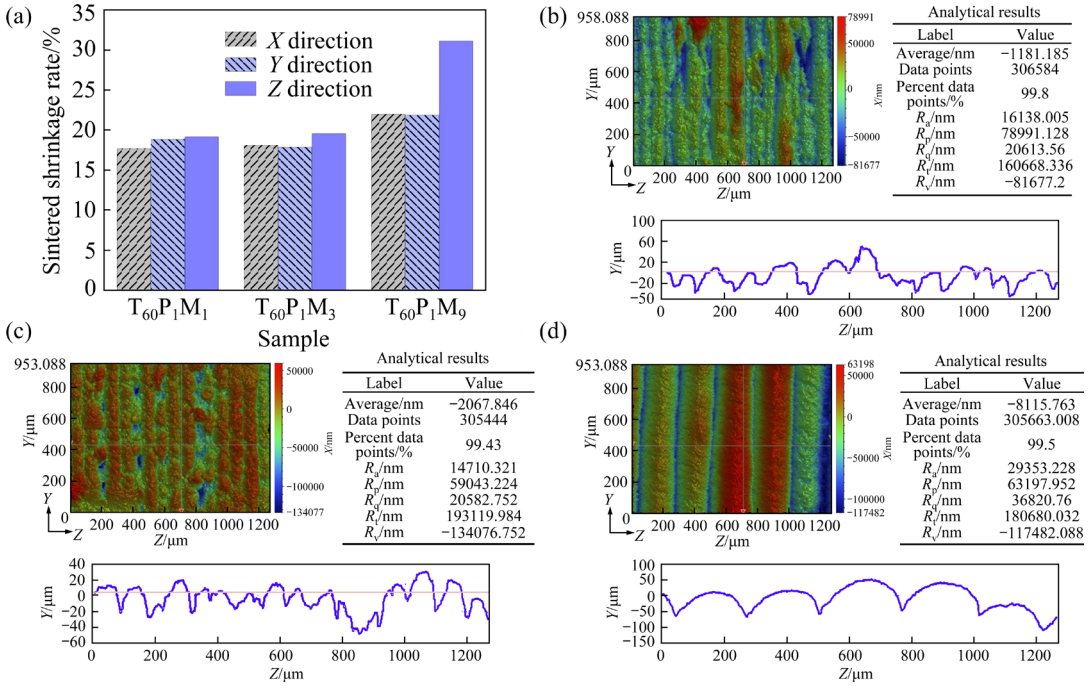

Fig. 5 Sintered shrinkage rate and surface roughness of WC−9Co cemented carbide prepared using MEX−WIP−DS: (a) Sintered shrinkage rate; (b−d) Surface roughness (*Y*−*Z* plane)

shrinkage rate of sintered sample $T_{60}P_1M_9$ is approximately 22.0% in the horizontal direction (*X* and *Y* directions) but reaches up to 31.1% in the vertical direction (*Z* direction). This phenomenon may be caused by the combined action of sintering pressure and gravity. The roughness of sintered samples $T_{60}P_1M_1$, $T_{60}P_1M_3$, and $T_{60}P_1M_9$ on the *Y*−*Z* plane is presented in Figs. 5(b, c, d), respectively. The results indicate that, compared with the MEX−DS cemented carbide [17], the surface roughness of all three sintered samples has slightly decreased, with values of 16.14, 14.71, and 29.35 μm, respectively. This suggests that the WIP treatment of MEX greens does not adversely affect the surface roughness of sintered samples.

Figure 6 displays the morphology of complex-shaped WC−9Co cemented carbide parts prepared using the MEX−WIP−DS process. It is shown that the shape characteristics of the MEX green samples are well preserved following the WIP and DS stages (Figs. 6(a, b)). The results indicate that the green samples experience relatively uniform pressure in all directions during WIP, and the WIP process does not compromise the shape characteristics of these green samples. Integrating the green WIP process into MEX AM technology enables the efficient production of complex-shaped cemented carbide products.

(2) Pores and Co pools

Figure 7 presents the micro-CT images of internal defects and relative densities of sintered samples. The results indicate that no pores are

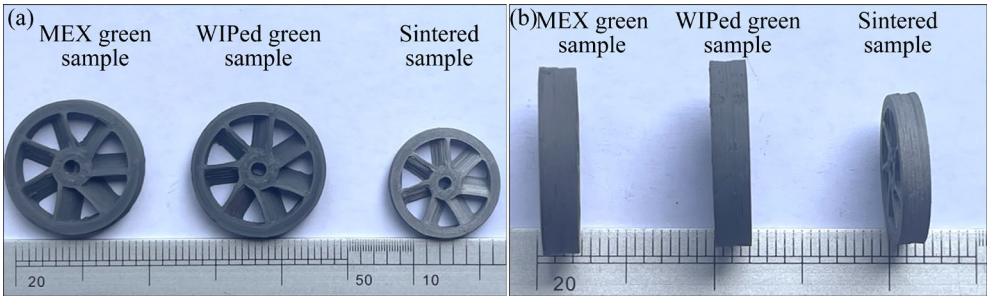

Fig. 6 Morphologies of sintered complex-shaped samples prepared using MEX−WIP−DS: (a) *X*−*Y* plane; (b) *X*−*Z* plane

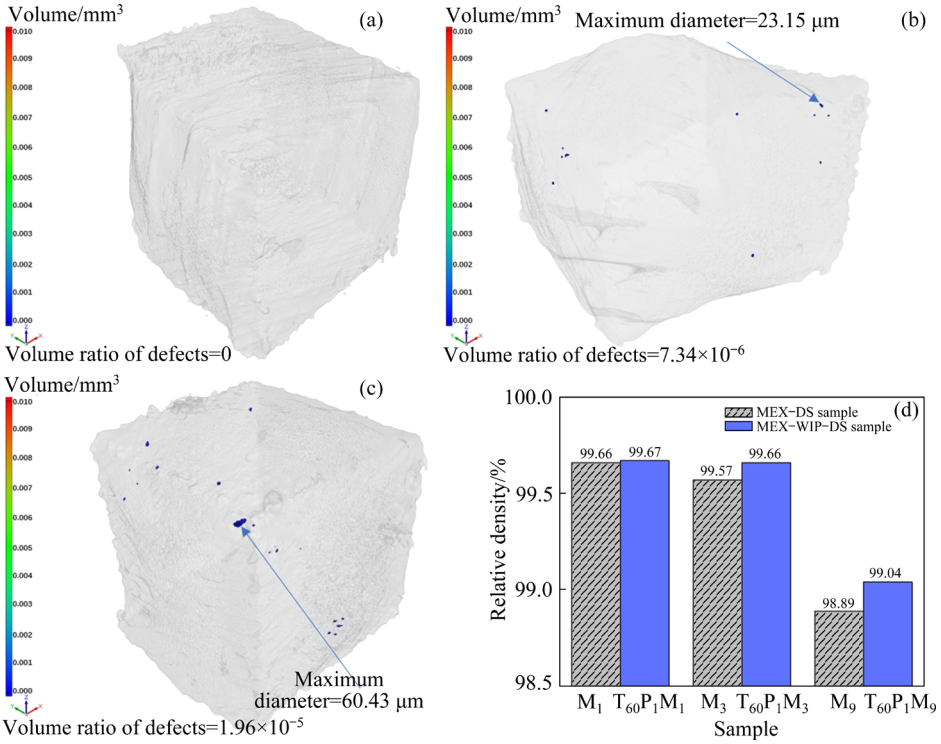

Fig. 7 Micro-CT images of internal defects (a−c) and relative densities (d) of sintered samples: (a) Sample $T_{60}P_1M_1$; (b) Sample $T_{60}P_1M_3$; (c) Sample $T_{60}P_1M_9$; (d) Relative densities of sintered samples prepared via MEX−DS and MEX−WIP−DS

observed inside the sintered sample $T_{60}P_1M_1$ (Fig. 7(a)), which is consistent with our previous research [17]. Compared with the sintered sample M_3 prepared by MEX−DS [17], the morphology of pores within $T_{60}P_1M_3$ shows no significant change (Fig. 7(b)); however, there is a notable decrease in the volume ratio (volume fraction, calculated by dividing the defect volume by the sample volume) of pores from 4.59×10^{-5} to 7.34×10^{-6}, as well as a reduction in the maximum diameter of the pores from 226 to 23.15 μm, resulting in decreases of 83.8% and 89.8%, respectively. Compared with the elongated through-going pores observed in sintered sample M_9 [17], the morphology of pores within $T_{60}P_1M_9$ has significantly changed (Fig. 7(c)). These pores now exhibit a flattened circular shape, with visible decreases in both volume ratio (from 6.41×10^{-5} to 1.96×10^{-5}) and maximum size (from 248 to 60.43 μm), corresponding to reductions of 69.4% and 75.6%, respectively. The relative densities of the sintered samples are depicted in Fig. 7(d). The results indicate that the influence of WIP on the relative density of MEX−DS samples is consistent with that of MEX greens. Specifically, compared with MEX green M_1, the relative density of WIPed green $T_{60}P_1M_1$ only increases by 0.15%. Therefore, the relative density of the sintered sample $T_{60}P_1M_1$ prepared from a nearly fully dense WIPed green increases by only 0.01%. Correspondingly, compared with MEX greens M_3 and M_9, the relative density of WIPed green $T_{60}P_1M_3$ and $T_{60}P_1M_9$ increases more significantly, and thus the relative densities of sintered samples $T_{60}P_1M_3$ and $T_{60}P_1M_9$ increase by 0.09% and 0.15%, respectively. The above results suggest that green WIP can significantly reduce the size and number, and alter the morphology of pores in MEX−DS cemented carbides, ultimately leading to an increase in their relative densities.

Figure 8 shows the SEM images of the pores and Co pools in sintered samples (*X*−*Z* plane) of WC−9Co cemented carbide prepared using MEX−DS and MEX−WIP−DS, respectively. Only partial sintered samples appear the defects of pores, Co pools, or Co-rich regions. In detail, no visible pores or interlayer bonding defects are observed in the MEX green sample M_1; consequently, neither the MEX−DS sample M_1 nor the MEX−WIP−DS sample $T_{60}P_1M_1$ exhibits any pores, Co pools, or other defects. The MEX green sample M_3 contains some small-sized pores; as a result, a few ultra-small-sized pores are also presented in the MEX−DS sample M_3, while no visible pores are observed in the MEX−WIP−DS sample $T_{60}P_1M_3$. In the MEX green sample M_9, a large number of triangular or wedge-shaped stacked pores cannot be eliminated through the DS process. Consequently, these pores persist in the sintered sample M_9 as residual sintered pores. In contrast, due to the morphological change of pores in WIPed green

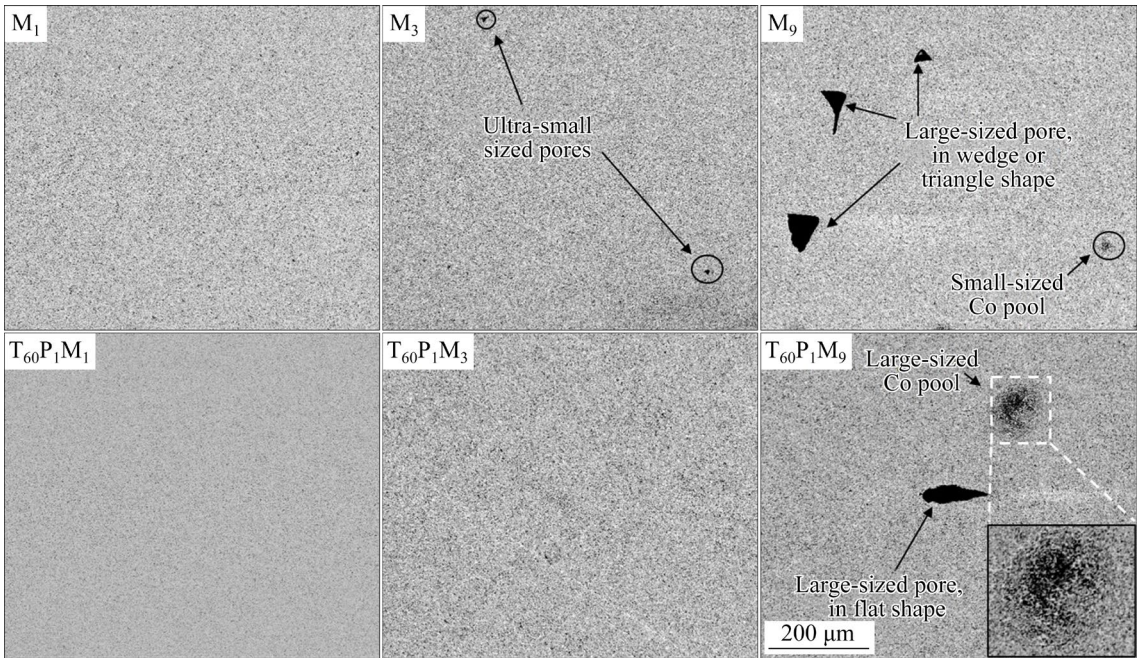

Fig. 8 SEM images of pores and Co pools in sintered samples (*X*−*Z* plane) prepared via MEX−DS and MEX−WIP−DS

sample $T_{60}P_1M_9$ (Fig. 2), the pore morphologies in the sintered sample $T_{60}P_1M_9$ have changed to a flattened shape.

As shown in Fig. 8, in comparison with the other sintered samples, only the sintered samples M_9 and $T_{60}P_1M_9$ exhibit dot-liked Co pools, suggesting that their formation may be closely related to the green large-sized defects. During the liquid phase sintering of WC−Co cemented carbides, eutectic reaction occurs between WC and Co to form a liquid phase. The sintered body undergoes significantly sintered shrinkage due to particle rearrangement by capillary force and dissolution−precipitation processes. Concurrently, the internal small-sized pores, microcracks, and interconnected channels formed by debinding are effectively filled and healed through the rearrangement and dissolution−precipitation of WC particles. However, around the large-sized pores, liquid-phase Co continuously enriches due to capillary force, establishing a new chemical equilibrium with the surrounding matrix [23,25]. With the increase of sintering temperature, the content of liquid phase increases significantly. Under the influence of sintering pressure, liquid-phase Co undergoes further migration and evaporation [26], causing the concentration of Co vapor around the pores to reach saturation gradually. During the cooling process, the abundant liquid-phase Co and Co vapor continuously deposit and solidify around the large-sized pores, eventually leading to the formation of Co-rich regions or Co pools inside or around the pores. Therefore, applying WIP treatment to MEX green is beneficial for reducing or eliminating the pore defects in the sintered samples, but it still needs to optimize the process for eliminating the defect of Co pool or Co-rich region.

3.2.2 Sintered microstructure

(1) Phases

The phases and elemental distribution EDS analysis results of the sintered samples are shown in Fig. 9. The results indicate that there is no significant difference in the elemental distribution between the sintered samples prepared by the MEX−WIP−DS and those prepared by the MEX−DS. Similar to the sintered samples M_1 and M_3 prepared using the MEX−DS process, the sintered samples $T_{60}P_1M_1$ and $T_{60}P_1M_3$ prepared via the MEX−WIP−DS process exhibit a typical microstructure of WC−Co cemented carbides, composed of WC and Co binder phases. In these samples, the dark regions correspond to the Co binder phase, while the bright regions represent the WC hard phase. The Co phase is dispersed around the WC phases in a reticular structure, which enhances the mechanical properties of the cemented carbide through plastic deformation and bridging effects. Consistent with Fig. 8, EDS analysis reveals the formation of large-sized Co pools in the sintered samples M_9 and $T_{60}P_1M_9$, suggesting that the WIP process does not significantly mitigate the Co pool defects.

(2) Grain morphology and size

Figure 10 shows the SEM images of the WC grain morphology of sintered samples prepared using the MEX−DS and MEX−WIP−DS after corrosion. It is revealed that the green WIP does not

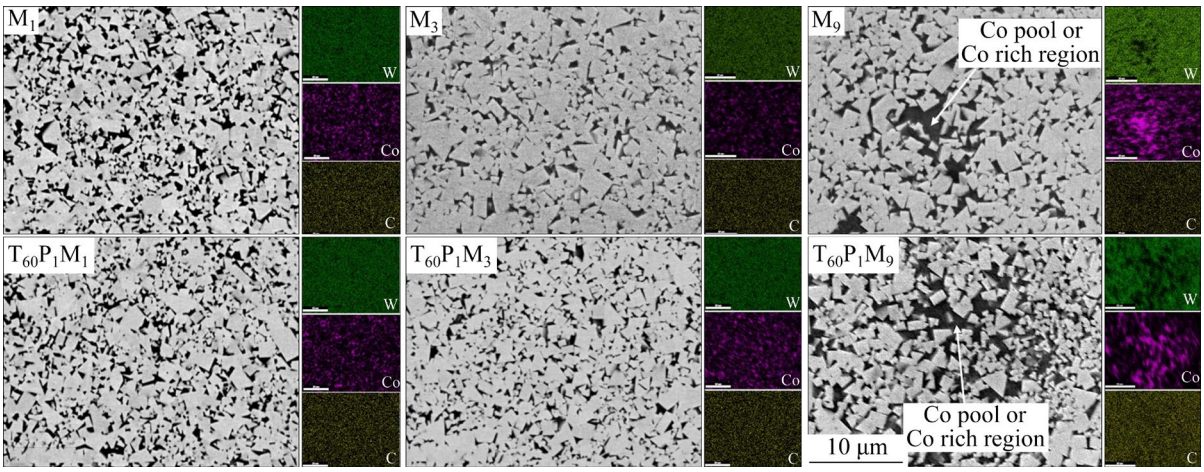

Fig. 9 Phases and elemental distribution EDS analysis results of sintered samples prepared via MEX−DS and MEX−WIP−DS

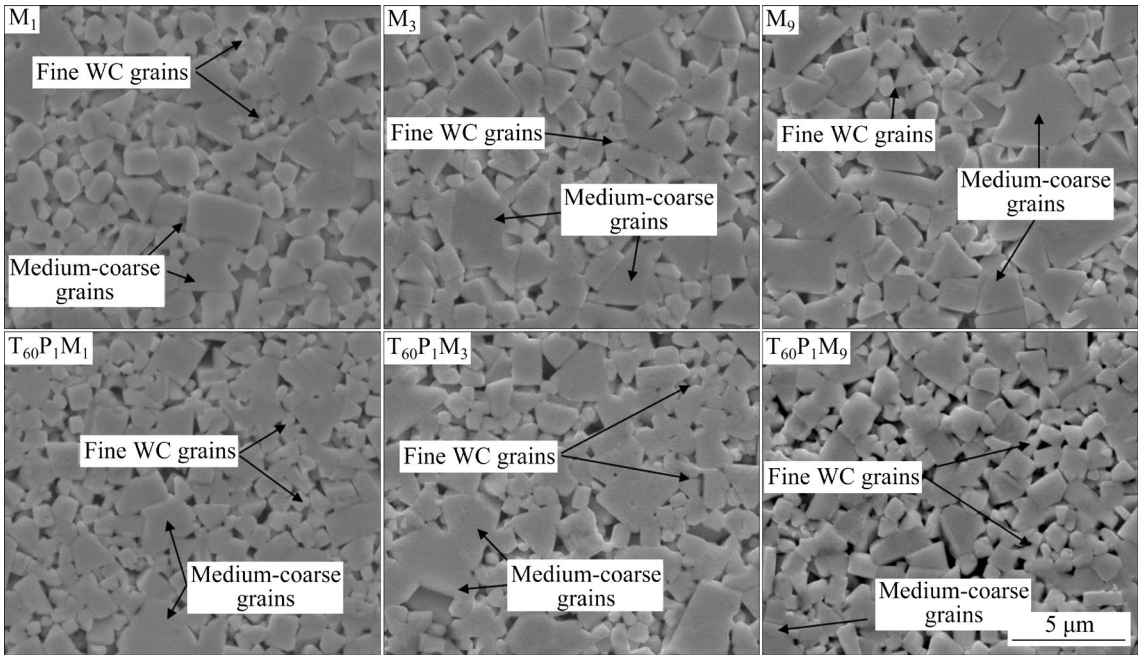

Fig. 10 SEM images of WC grains in sintered samples prepared via MEX−DS and MEX−WIP−DS (after corrosion)

significantly affect the morphology of WC grains in the sintered samples. The grains of all the sintered samples consist of dispersed medium-coarse grains and fine grains of WC, without any signs of grain agglomeration. Some WC grains exhibit a typical truncated triangular prism shape with rounded tips, while others show hexagonal plate-like morphology. The WC grains are characterized by a hexagonal crystal structure and display anisotropic properties, indicating that grains with varied morphologies and orientations possess notably different mechanical properties. Notably, the prismatic shape represents the equilibrium morphology of WC grains. According to the Hall−Petch formula [27], plate-like grains contribute to the enhancement of the hardness of cemented carbides by reducing the WC grain height. Furthermore, in comparison with the truncated triangular prismatic grains, the plate-like grains reduce the contact interface of WC grains, increasing the likelihood that crack tips align with the basal plane of WC grains. This phenomenon may hinder the blunting of crack tips, leading to intergranular fracture upon the breakage of the cemented carbide.

Figure 11 illustrates the IPF images and grain size distribution of sintered samples prepared via the MEX−DS and MEX−WIP−DS. The results show that all the sintered samples exhibit a microstructure characterized by a dispersed distribution of medium-coarse and fine WC grains. Specifically, the fine grains measure approximately 0.4−0.5 μm, while the medium-coarse grains can attain sizes of 6−7 μm. Moreover, the average grain sizes of the sintered samples produced by both processes exceed those of similar products prepared from the same powder batch via the compacting and sintering process [17]. Specifically, the average grain sizes of sintered samples M_1, M_3, and M_9, prepared using the MEX−DS process, range from 1.49 to 1.60 μm; In contrast, the average grain sizes of sintered samples $T_{60}P_1M_1$, $T_{60}P_1M_3$, and $T_{60}P_1M_9$, produced using the MEX−WIP−DS process, show a slight reduction and range from 1.31 to 1.45 μm.

The grain growth of WC−Co cemented carbides is primarily driven by the dissolution−precipitation effect. During the liquid-phase sintering stage, small WC continuously dissolves into liquid-phase Co to form tungsten (W) and carbon (C) atoms, and these W and C atoms in liquid-phase Co precipitate and grow on the surface of undissolved WC grains. Due to higher content of liquid-phase Co, the growth resistance of WC grains around pores is relatively low. Therefore, for the MEX greens with pore defects, the enrichment of liquid-phase Co, driven by capillary force, facilitates the further growth of WC grains by precipitating W and C atoms onto large WC grains adjacent to the pores. Therefore, employing the

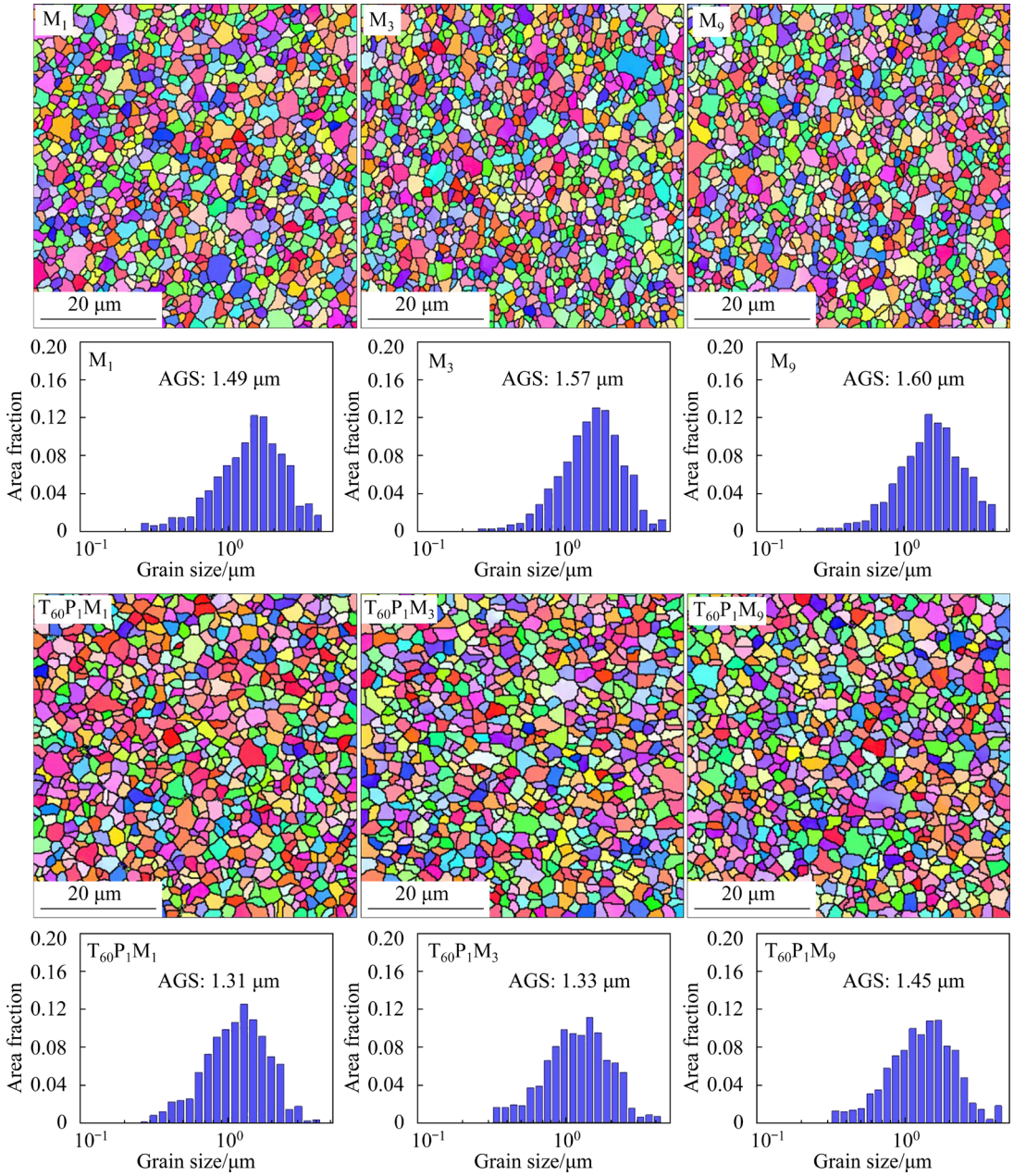

Fig. 11 IPF images and grain size distribution of sintered samples prepared via MEX−DS and MEX−WIP−DS (AGS: Average grain size)

green WIP to reduce the internal pore defects of MEX greens is conducive to promoting the uniform distribution of liquid-phase Co during sintering. This approach ultimately can reduce the number of large WC grains in the sintered samples, leading to a slight decrease in the average size of WC grains.

3.3 Mechanical properties

3.3.1 Hardness

Figure 12 displays the mechanical properties of WC−9Co cemented carbides prepared by the MEX−DS and MEX−WIP−DS. Figure 12(a) shows that the Vickers hardness of the sintered samples M_1, M_3, and M_9 are HV_{30} 1506, HV_{30} 1501, and HV_{30} 1497, respectively. In contrast, those of the sintered samples $T_{60}P_1M_1$, $T_{60}P_1M_3$, and $T_{60}P_1M_9$ are HV_{30} 1508, HV_{30} 1498, and HV_{30} 1494, respectively, which suggests that the green WIP treatment has no significant effect on the Vickers hardness of sintered samples. Cemented carbides are hard and brittle materials, and their hardness is primarily influenced by metallurgical defects and grain size. The WIP process is beneficial for achieving a relatively dense sintered microstructure,

but the hardness of these sintered samples is more sensitive to grain size. Therefore, the average grain sizes of sintered samples prepared by these two processes are quite similar, resulting in close hardness values with a variation rate of 0.1%−0.2%.

3.3.2 Transverse rupture strength

Figure 12(b) illustrates the transverse rupture strength of WC−9Co cemented carbides prepared by the MEX−DS and MEX−WIP−DS. The data indicate that, compared with the WC−9Co cemented carbides fabricated using MEX−DS, those cemented carbides prepared by MEX−WIP−DS exhibit a significant enhancement in transverse rupture strength. Notably, the sintered sample $T_{60}P_1M_9$, prepared from a green with more defects, shows the most pronounced enhancement in the transverse rupture strength. In contrast, the sintered sample M_1 achieves nearly full density, and the strengthening effect of WIP on its transverse rupture strength is relatively limited.

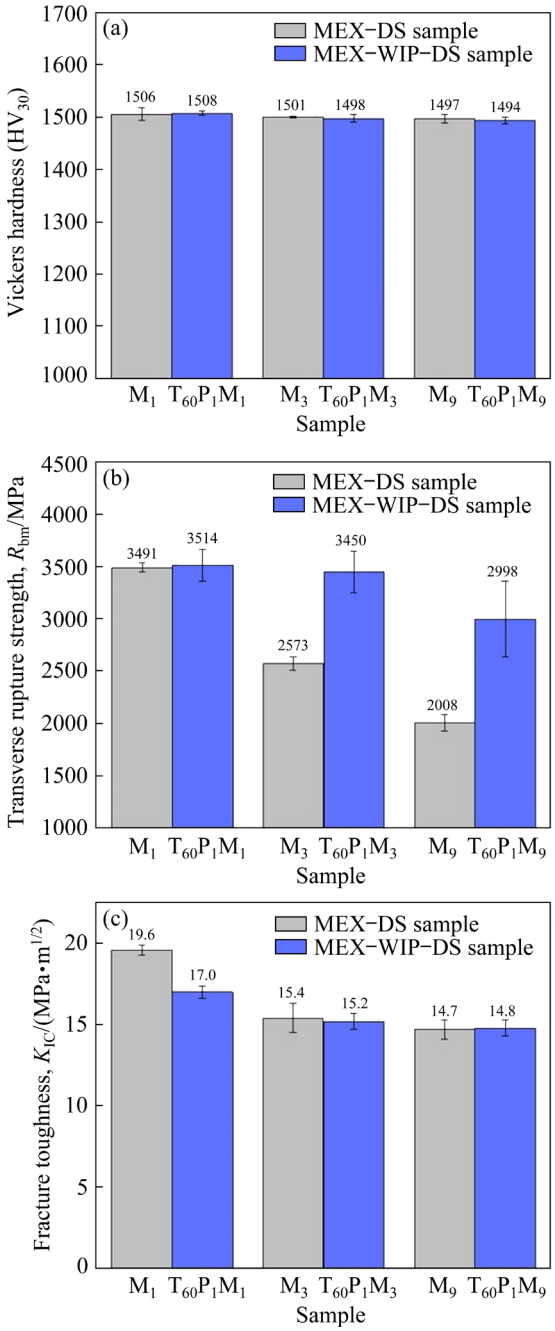

Fig. 12 Mechanical properties of WC−9Co cemented carbide prepared via MEX−DS and MEX−WIP−DS: (a) Vickers hardness; (b) Transverse rupture strength; (c) Fracture toughness

Specifically, the transverse rupture strength of the sintered sample $T_{60}P_1M_1$ is approximately 3514 MPa, reflecting an increase of about 0.7% compared with sample M_1. On the contrary, the sintered sample M_3 contains some small pores, resulting in a relatively diminished transverse rupture strength; consequently, the pore defects in sintered sample $T_{60}P_1M_3$ are significantly reduced after green WIP, leading to an increase in its transverse rupture strength to 3450 MPa. This represents an enhancement of approximately 34.1% compared with sintered sample M_3 and is comparable to similar products produced by powder metallurgy. Due to a high number fraction of stacked pores in the green sample M_9, the sintered sample M_9 displays the lowest transverse rupture strength. Consequently, the transverse rupture strength of sintered sample $T_{60}P_1M_9$ is significantly enhanced to 2998 MPa, indicating an increase of approximately 49.3%. The results illustrate that for stacked pores and interlayer bonding defects in MEX cemented carbide greens, which severely compromise the transverse rupture strength of the sintered samples, incorporating green WIP could effectively mitigate these defects and improve the strength of the sintered samples.

Figure 13 presents the fracture surface images of sintered samples prepared using the MEX−DS and MEX−WIP−DS. Similar to the sintered sample M_1 prepared using the MEX−DS, the fracture surface of sintered sample $T_{60}P_1M_1$ prepared using the MEX−WIP−DS exhibits a uniform distribution of the Co phase in a reticular structure, with no visible pores or cracks. The fracture morphology indicates that the primary fracture mode of fine grains is intergranular fracture, along the WC/Co phase and the WC/WC grain boundaries. Compared with the sintered sample M_3 characterized by some small-sized pores, the fracture surface of the sintered

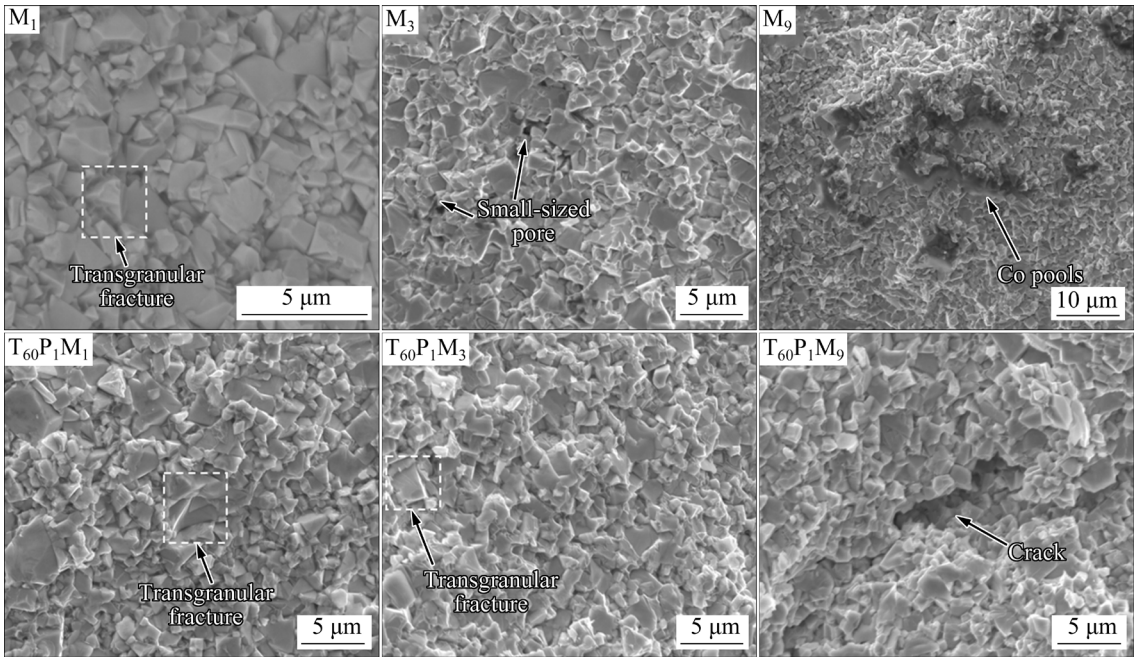

Fig. 13 Transverse rupture fracture morphologies of sintered samples prepared via MEX−DS and MEX−WIP−DS

sample $T_{60}P_1M_3$ shows no visible pores or cracks, albeit with some medium-coarse grains displaying trans-granular fractures. Furthermore, in samples containing Co pool defects, the Co phase tends to fracture preferentially due to its low strength, thereby serving as the fracture source during transverse fracture. As a result, Co pools are evident on the fracture surface of sintered sample M_9. However, Fig. 13 shows that the fracture surface of sintered sample $T_{60}P_1M_9$ does not exhibit distinct Co pools; instead, noticeable cracks are observed, which may be attributed to the sintering defects.

The transverse rupture strength of WC−Co cemented carbide is influenced by the Co content and average size of WC grains, as well as porosity and cracks. Under the condition of other factors being the same, its strength σ is very sensitive to porosity ε and the average grain size D of WC, and its relationship can be described by Eq. (2) [28]:

$$\sigma=K\cdot D^{-a}\cdot e^{-b\varepsilon} \quad (2)$$

where K, a, and b are constants. For the sintered samples M_1 and M_3 of WC−Co cemented carbides with high density, the impact of green WIP process on improving sintered defects and reducing average grain sizes of sintered samples is limited. Consequently, its strengthening effect on the transverse rupture strength is relatively minor. In contrast, compared with the sintered sample M_9 characterized by a significant number of pore defects, the green WIP process reduces both pore size and quantity and significantly increases the relative density of sintered sample $T_{60}P_1M_9$, which is advantageous for altering the adjacency state of WC/WC grains and interfacial characteristics at grain boundaries of the sintered samples. As a result, it is possible to enhance the bonding strength at WC/WC interfaces, ultimately resulting in a notable enhancement in its transverse rupture strength.

3.3.3 Fracture toughness

Figure 12(c) presents the fracture toughness of WC−9Co cemented carbides prepared using the MEX−DS and MEX−WIP−DS. The results indicate that the fracture toughness of the sintered samples M_1, M_3, and M_9 prepared by the MEX−DS process is 19.6, 15.4 and 14.7 MPa·m$^{1/2}$, respectively. In contrast, the fracture toughness of the sintered samples $T_{60}P_1M_1$, $T_{60}P_1M_3$, and $T_{60}P_1M_9$ prepared by the MEX−WIP−DS process is 17.0, 15.2 and 14.8 MPa·m$^{1/2}$, respectively. Compared with M_1, the fracture toughness of $T_{60}P_1M_1$ shows a decrease (approximately 12.3%); whereas compared with M_3 and M_9, the fracture toughness of $T_{60}P_1M_3$ and $T_{60}P_1M_9$ does not change significantly.

For dense WC−Co cemented carbide, the grain size and mean free path of Co phase are significant factors influencing the fracture toughness. The fracture toughness and strength cannot be enhanced

simultaneously [29]. Herein, the mean free path of Co phase (λ) can be calculated by Eq. (3) [30]:

$$\lambda = \frac{2V_{Co}}{N_{WC/Co}} \tag{3}$$

where $N_{WC/Co}$ is the number of WC/Co interfaces per unit line length, and V_{Co} is the volume fraction of the Co phase.

By employing the grid method to measure the values of $N_{WC/Co}$ and V_{Co} from the SEM images of sintered samples (Fig. 8), the mean free path of Co phase for each sintered sample can be calculated, as listed in Table 3. The results show that, compared with the sintered samples M_1 and M_3, the mean free path of Co phase in the sintered samples $T_{60}P_1M_1$ and $T_{60}P_1M_3$, which undergo green WIP, slightly decreases, and the values of the mean free path of Co phase in these two samples are very close. However, due to the presence of the Co pool, the mean free path of Co phase in both the sintered sample M_9 without green WIP and the sintered sample $T_{60}P_1M_9$ with green WIP is relatively large, and these two values are almost identical.

WIP facilitates the displacement and rearrangement of particles in the MEX green through the flow and diffusion of plastic binder, thereby influencing the uniformity of microstructure and the mean free path of Co phase in the sintered samples. For the sintered samples that have achieved a dense and uniform microstructure, their fracture toughness is more sensitive to the grain size and mean free path of Co phase. Compared with the sintered sample M_1, the sintered sample $T_{60}P_1M_1$ exhibits a slightly reduced average grain size and mean free path of Co phase, resulting in a minor decrease in its fracture toughness. In comparison to the sintered samples M_3 and M_9, which contain numerous sintered pores, the slight reduction of WC grain size in the sintered samples $T_{60}P_1M_3$ and $T_{60}P_1M_9$ with green WIP may reduce their fracture toughness. However, the pore size and quantity in these two sintered samples are significantly reduced, and their relative densities are noticeably increased, which is advantageous for enhancing their fracture toughness [31]. Therefore, due to the combined effects of these factors, the green WIP treatment can maintain the fracture toughness of the sintered samples $T_{60}P_1M_3$ and $T_{60}P_1M_9$ at a relatively stable level.

Figure 14 displays the crack images from the hardness test of sintered samples prepared using MEX−WIP−DS. The results indicate that the cracks in the sintered sample $T_{60}P_1M_1$ predominantly exhibit an intergranular extension along the WC/Co phase boundaries, with a relatively tortuous propagation path. However, a small amount of trans-granular fracture is also observed near some medium-coarse grains. Since crack propagation along the WC/Co phase boundaries consumes more energy than fracture along the WC/WC grain boundaries, the increase in the contiguity of WC grains can facilitate further crack propagation along the WC/Co phase boundaries. Furthermore, it can be observed in Fig. 14 that the direction of crack propagation in all the sintered samples is primarily influenced by the thickness of Co phase. The region with a relatively thick Co phase exhibits high plastic deformation ability, which promotes crack-tip blunting, thereby impeding the crack propagation and enhancing the fracture toughness.

Table 3 Mean free path of Co phase of sintered samples

Sample	M_1	M_3	M_9	$T_{60}P_1M_1$	$T_{60}P_1M_3$	$T_{60}P_1M_9$
Mean free path of Co phase/μm	0.45	0.47	0.61	0.40	0.41	0.62

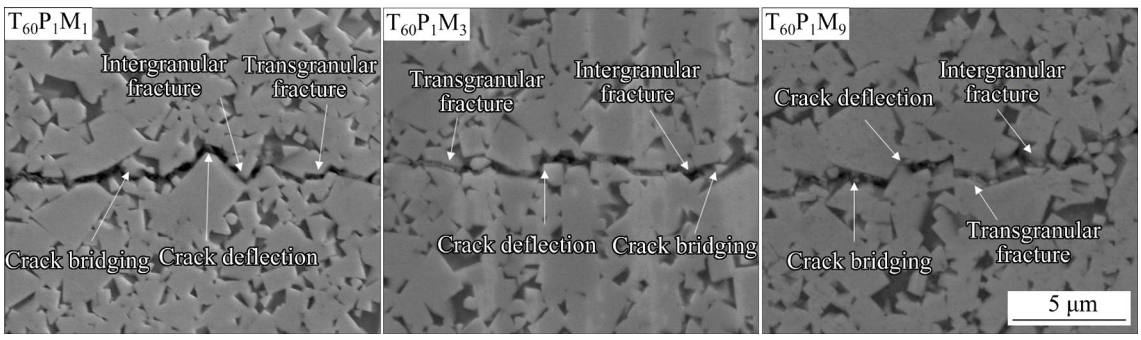

Fig. 14 Crack images from hardness test of sintered samples prepared using MEX−WIP−DS

Conversely, the region with a relatively thin Co phase has limited plastic deformation ability, making the alloy more prone to brittle fracture. Such brittle fractures can reduce fracture toughness and may cause crack deflection during propagation.

Table 4 presents the mechanical properties of cemented carbides with similar compositions prepared by conventional powder metallurgy and sinter-based AM technologies recently reported. The results indicate that although the sinter-based AM technology can produce WC−Co cemented carbides with mechanical properties comparable to those of the conventional powder metallurgy counterparts, the difficult-to-eliminate pores and low interlayer bonding strength in the cemented carbide green require overly stringent parameters for the sinter-based AM processes, which in turn severely reduces the production efficiency. In this study, the MEX cemented carbide greens prepared with different MEX parameters are subjected to WIP treatment and sintered samples are obtained with a hardness of HV_{30} 1494−1508, a significant improvement in transverse rupture strength of 2998−3514 MPa, and a fracture toughness of 14.8−17.0 MPa·$m^{1/2}$. The overall mechanical properties are superior to those of similar products prepared by other AM processes reported recently and are comparable to those of powder metallurgy counterparts. In summary, the green WIP process can reduce the defects in the MEX cemented carbide

Table 4 Mechanical properties of WC−Co cemented carbides prepared via various techniques reported recently

Preparation process	Material	Grain size/μm	Relative density/%	Hardness	R_{bm}/MPa	K_{IC}/(MPa·$m^{1/2}$)
Compacting and sintering [32,33]	WC−TiC−Ti(C,N)−9Co	1.56	99.57	HV_{20} 1227	2519	12−12.5
Compacting and sintering [32]	WC−TiC−Ti(C,N)−$MWCNT_s$−9Co	1.35−1.59	99.72−100.09	HV_{20} 1191−1330	2400−2798	13−16.5
Compacting and sintering [33]	WC−TiC−Ti(C,N)−SiC_w−9Co	1.46	99.39−100.03	HV_{20} 1294	2757	15.02
Compacting and sintering [34]	WC−9Co	8.7 (Ultra-coarse grain)	−	HV 927	1952	22.35
Compacting and sintering [34]	WC−TaC−9Co	6	−	HV 1124	2466	19.34
Compacting and sintering [35,36]	WC−10Co	0.46−0.57	Full density	1655−1688 kg/mm^2	3921−4475	−
Compacting and sintering−HIP [37]	WC−VC−8Co	5.3	99	1243	2638	16.4
BJT−DS−HIP [38]	WC−12Co	8 (Ultra-coarse grain)	99.3	HV_{10} (1205±12)	2257±28	−
BJT−DS−HIP [3]	WC−10Co	6	Full density	HV_{30} 1119	2231	18.8
BJT−DS−HIP [3]	WC−12Co	6	Full density	HV_{30} 1050	2684	19.4
SG−3DP−DS−HIP [39]	WC−12Co	−	99.9	HV_{30} (1308±10)	−	12.1±0.3
3DGP−DS [40]	WC−20Co	−	99.9	HRA 87.7	2612.8	−
MEX−DS[16]	WC−10Co	−		16.5 GPa	−	10.1
MEX−DS [13−15]	WC−8Co	2.12−2.39	99.1−99.3	HV_{30} (1313−1362)	1644−1861	7.27
MEX−DS [17] (this work)	WC−9Co	1.32−1.59	98.89−99.66	HV_{30} (1497−1525)	2008−3492	14.7−20.4
MEX−WIP−DS (this work)	WC−9Co	1.31−1.45	99.04−99.67	HV_{30} (1494−1508)	2998−3514	14.8−17.0

greens, thereby reducing the sintered defects and improving the microstructure uniformity of cemented carbides prepared by the MEX−DS process, ultimately enhancing their mechanical properties. Therefore, integrating green WIP into MEX−DS process could effectively broaden the process window for the MEX process of greens, and facilitate the efficient preparation of WC−Co cemented carbide products with excellent overall mechanical properties prepared by the MEX AM technology.

4 Conclusions

(1) Green WIP can reduce the defects associated with stacked pores and interlayer bonding defects in MEX cemented carbide greens, leading to an increase in relative density and transverse rupture strength of cemented carbide greens. Specifically, conducting WIP at 60 °C and 1 MPa can enhance the relative density of MEX WC−9Co cemented carbide greens from 97.14%−98.45% to 97.68%−98.60%, and increase the transverse rupture strength from 9.4−14 MPa to 11.6−16.3 MPa.

(2) Green WIP significantly reduces the porosity and maximum pore size of MEX−DS WC−9Co cemented carbides with internal pore defects by 83.8% and 89.8%, respectively. Due to the relatively uniform pressure applied in all directions, the surface quality and structure integrity of complex-shaped cemented carbide parts can be preserved well.

(3) Green WIP can enhance the overall mechanical properties of MEX−DS WC−9Co cemented carbides by improving the sintered defects and the uniformity of microstructure, as well as influencing the average grain size and the mean free path of Co phase. Compared with the MEX−DS WC−9Co samples, the hardness of MEX−WIP−DS samples remains essentially unchanged, ranging from HV_{30} 1494 to HV_{30}1508, the transverse rupture strength can be increased by as much as 49.3%, reaching values between 2998 and 3514 MPa, and the fracture toughness is maintained at a high level, ranging from 14.8 to 17.0 $MPa·m^{1/2}$.

(4) The mechanical properties of WC−9Co prepared via MEX−WIP−DS are significantly superior to those of comparable products prepared using other AM methods reported recently and are comparable to those of powder metallurgy counterparts. It can be concluded that the integration of green WIP into MEX−DS reduces defects in MEX greens and broadens the processing window for MEX. This facilitates the elimination of sintered defects and improves the overall mechanical properties of MEX AM cemented carbides.

CRediT authorship contribution statement

Cai CHEN: Writing − Original draft, Review & editing, Data curation, Methodology, Formal analysis; **Run-xing ZHOU:** Data curation, Formal analysis, Formal analysis; **Zu-ming LIU:** Writing − Review & editing, Data curation, Methodology, Funding acquisition, Project administration, Resources, Supervision, Conceptualization; **Yong-xia LI:** Writing − Review & editing, Methodology, Formal analysis; **Dan ZOU:** Writing – Review & editing, Methodology, Formal analysis; **Yi-ming CHANG:** Data curation, Formal analysis; **Xu-lin CHENG:** Data curation, Formal analysis.

Declaration of competing interest

The authors declare that they have no known competing financial interests or personal relationships that could have appeared to influence the work reported in this paper.

Acknowledgments

This work was supported by the Key Project of Chinese Academy of Engineering (No. 2019-XZ-11), the General Project of Chinese Academy of Engineering (No. 2023-XY-18), the Open Fund of National Joint Engineering Research Center for Abrasion Control and Molding of Metal Materials of China (No. HKDNM201907), and the Independent Project of State Key Laboratory of Powder Metallurgy, China.

References

[1] HUANG Bai-yun, WEI Wei-feng, LI Song-lin, ZHANG Li, LI Li-ya, LIU Feng, LI Rui-di. Development of modern powder metallurgy materials and technology [J]. The Chinese Journal of Nonferrous Metals, 2019, 29(9): 1917−1933. (in Chinese)

[2] OSMAN H, LIU Lin. Additive manufacturing of high-entropy alloy composites: A review [J]. Transactions of Nonferrous Metals Society of China, 2023, 33(1): 1−24.

[3] WOLFE T A, SHAH R M, PROUGH K C, TRASORRAS J L. Coarse cemented carbide produced via binder jetting 3D

printing [J]. International Journal of Refractory Metals and Hard Materials, 2023, 110: 106016.

[4] WOLFE T A, SHAH R M, PROUGH K C, TRASORRAS J L. Binder jetting 3D printed cemented carbide: Mechanical and wear properties of medium and coarse grades [J]. International Journal of Refractory Metals and Hard Materials, 2023, 113: 106197.

[5] WU Jin-bo, LIU Ye, ZHANG Wei, ZHANG Wei, GAO Xuan, LUO Yang, ZHOU Cheng-shang. Controlling η phase distribution and its effects on carburized graded cemented carbides via extrusion additive manufacturing [J]. Ceramics International, 2024, 50(21): 44648−44658.

[6] KUMAR S. Process chain development for additive manufacturing of cemented carbide [J]. Journal of Manufacturing Processes, 2018, 34: 121−130.

[7] XING Ming, WANG Hai-bin, ZhAO Zhi, LU Hao, LIU Chao, LIN Liang-liang, WANG Ming-sheng, SONG Xiao-yan. Additive manufacturing of cemented carbides inserts with high mechanical performance [J]. Materials Science and Engineering A, 2022, 861: 144350.

[8] ZHAO Yu-xia, WANG Hang, ZHANG Li, LI Xiao-feng, GUO Ziao, ZHANG Jin-fang, YI Deng-hao, LIU Bin, BAI Pei-kang. Study on the microstructure and properties of WC−12Co cemented carbide fabricated by selective laser melting [J]. Journal of Materials Research and Technology, 2022, 20: 3512−3521.

[9] WANG Jian-hong, HAN Yu-long, ZHAO Yu-xia, LI Xiao-feng, YI Deng-hao, GUO Ziao, CAO Yuan-kui, LIU Bin, TANG H P. Microstructure and properties of WC−12Co cemented carbide fabricated via selective electron beam melting [J]. International Journal of Refractory Metals and Hard Materials, 2022, 106: 105847.

[10] BOSE A, REIDY J P, PÖTSCHKE J. Sinter-based additive manufacturing of hardmetals: Review [J]. International Journal of Refractory Metals and Hard Materials, 2024, 119: 106493.

[11] CHEN Cai, HUANG Bo-yun, LIU Zu-ming, LI Yong-xia, ZOU Dan, LIU Tao, CHANG Yi-ming, CHEN Lei. Additive manufacturing of WC−Co cemented carbides: Process, microstructure, and mechanical properties [J]. Additive Manufacturing, 2023, 63: 103410.

[12] SUN Yi, YI Zhong-huai, SHEN Ting, XIONG Hui-wen, KANG Xiao, ZHANG Lei, ZHOU Ke-chao. Microstructure and mechanical properties of 7075 aluminum alloy prepared by metal fused deposition modeling [J]. Transactions of Nonferrous Metals Society of China, 2024, 34(7): 2108−2119.

[13] ZHAO Zai, LIU Ru-tie, CHEN Jie, XIONG Xiang. Carbon control and densification of WC−8%Co fabricated by extrusion-based additive manufacturing under pressureless sintering [J]. Materials Today Communications, 2023, 36: 106866.

[14] ZHAO Zai, LIU Ru-tie, CHEN Jie, XIONG Xiang. Additive manufacturing of cemented carbide using analogous powder injection molding feedstock [J]. International Journal of Refractory Metals and Hard Materials, 2023, 111: 106095.

[15] ZHAO Zai, LIU Ru-tie, CHEN Jie, XIONG Xiang. Material extrusion printing of WC-8%Co cemented carbide based on partly water-soluble binder and post-processing [J]. Journal of Materials Research and Technology, 2024, 29: 4394−4405.

[16] KIM H, KIM J I, KIM Y D, JEONG H, RYU S S. Material extrusion-based three-dimensional printing of WC−Co alloy with a paste prepared by powder coating [J]. Additive Manufacturing, 2022, 52: 102679.

[17] CHEN Cai, HUANG Bo-yun, LIU Zu-ming, CHEN Lei, LI Yong-xia, ZOU Dan, CHANG Yi-ming, CHENG Xu-lin, ZHOU Run-xing, LIU Ye. Material extrusion additive manufacturing of WC−9Co cemented carbide [J]. Additive Manufacturing, 2024, 86: 104203.

[18] PARK S J, PARK S J, SON Y, AHN I H. Reducing anisotropy of a part fabricated by material extrusion via warm isostatic pressure (WIP) process [J]. Additive Manufacturing, 2022, 55: 102841.

[19] XIAO Zhi-yu, LI Yuan-yuan, NI Dong-hui. Densification mechanism of warm compaction in powder metallurgy [J]. Materials Science and Engineering of Powder Metallurgy, 2006, 11(2): 85−90. (in Chinese)

[20] ZHANG Tian, TAN Yuan-qiang, XU Yang-li, LIU Chao. A thermal-initiated monomer binder enhancing green strength with low binder saturation for binder jetting additive manufacturing of cemented carbide [J]. International Journal of Refractory Metals and Hard Materials, 2024, 118: 106494.

[21] PARK S J, KIM D H, JU H G, PARK S J, HONG S, SON Y, AHN I H. Increased interlayer bonding strength of short carbon fiber composite fabricated by material extrusion via warm isostatic pressing (WIP) process [J]. Journal of Materials Research and Technology, 2023, 25: 3610−3623.

[22] GARZON-HERNANDEZ S, GARCIA-GONZALEZ D, JÉRUSALEM A, ARIAS A. Design of FDM 3D printed polymers: An experimental-modelling methodology for the prediction of mechanical properties [J]. Materials & Design, 2020, 188: 108414.

[23] CÔTÉ R, DEMERS V, DEMARQUETTE N R, CHARLON S, SOULESTIN J. A strategy to eliminate interbead defects and improve dimensional accuracy in material extrusion 3D printing of highly filled polymer [J]. Additive Manufacturing, 2023, 68: 103509.

[24] YI Zhong-huai, SHEN Ting, XIONG Hui-wen, KANG Xiao, ZHANG Lei, ZHOU Ke-chao. Strong and densified 3D metal-ceramic composite with strengthened layer structure by material extrusion additive manufacturing [J]. Additive Manufacturing, 2024, 84: 104136.

[25] TUNCER N, BOSE A. Solid-state metal additive manufacturing: A review [J]. JOM, 2020, 72(9): 3090−3111.

[26] MA Ming-yuan, DIAO Ying-chun, WANG Kai, ZHOU Xiang-kui, LI Guo-jian, WANG Qiang. Sintering behavior of WC−10Co−V(C,N) nanocrystalline gradient cemented carbide [J]. Ceramics International, 2023, 49(22, Part A): 35112−35122.

[27] LIAO Jiang-xiong, XU Chun-fang, NIE Ya. Evolution mechanism of grain morphology in WC−Co carbide and its effect on properties [J]. Cemented Carbide, 2018, 35(1): 63−68. (in Chinese)

[28] LI Ding. Study on the preparation process, microstructure and mechanical properties of ultrafine-grained WC−10Co cemented carbides [D]. Chengdu; Sichuan University, 2021. (in Chinese)

[29] ROULON Z, MISSIAEN J M, LAY S. Carbide grain growth in cemented carbides sintered with alternative binders [J]. International Journal of Refractory Metals and Hard Materials, 2020, 86: 105088.
[30] YANG Jian-gao, TAN Dun-qiang, CHEN Hao. Cemented carbide [M]. Changsha: Central South University Press, 2012. (in Chinese)
[31] MIN Fan-lu, YU Song-bai, WANG Sheng, YAO Zhan-hu, NOUDEM J G, LIU Si-jin, ZHANG Jian-feng. Preparation and properties of Ni-coated WC powder and highly impact resistant and corrosion resistant WC−Ni cemented carbides [J]. Transactions of Nonferrous Metals Society of China, 2022, 32(6): 1935−1947.
[32] JIANG Jun-peng, OUYANG Shui-lin, CHEN Hao, GUO Sheng-da, YIN Lei, TAN Zhuo-peng, SHI Hai-dong, ZHONG Zhi-qiang, QIU Lian-chang. Effect of MWCNTs on microstructure and properties of WC−9Co gradient cemented carbides [J]. Ceramics International, 2022, 48(13): 19295−19304.
[33] JIANG Jun-peng, OUYANG Shui-lin, ZHANG Sheng-zhou, ZHOU Ai-guo, CHEN Hao, YIN Lei, TAN Zhuo-peng, XING Sheng-hua, QIU Lian-chang, ZHONG Zhi-qiang. The role of SiCw in the microstructure and properties of WC−9Co gradient cemented carbide [J]. International Journal of Refractory Metals and Hard Materials, 2024, 120: 106554.
[34] SU Wei, SUN Ye-xi, YANG Hai-lin, ZHANG Xian-qi, RUAN Jian-ming. Effects of TaC on microstructure and mechanical properties of coarse grained WC−9Co cemented carbides [J]. Transactions of Nonferrous Metals Society of China, 2015, 25(4): 1194−1199.
[35] TANG Yan-yuan, CHEN Li-yong, YANG Qiu-min, ZHONG Zhi-qiang, XU Guo-zuan. Effect of a slight change in carbon content near the upper/lower limit on the microstructure and mechanical properties of WC−10Co cemented carbides [J]. International Journal of Refractory Metals and Hard Materials, 2021, 96: 105465.
[36] TANG Yan-yuan, ZHONG Zhi-qiang, YANG Qiu-min, WANG Hong-yun, XU Guo-zuan. Effect of carbon content on microstructure and mechanical properties of WC−10Co cemented carbides [J]. Rare Metals and Cemented Carbides, 2021, 49(6): 73−78, 93. (in Chinese)
[37] SU Wei, SUN Ye-xi, WANG Hui-feng, ZHANG Xian-qi, RUAN Jian-ming. Preparation and sintering of WC−Co composite powders for coarse grained WC−8Co hardmetals [J]. International Journal of Refractory Metals and Hard Materials, 2014, 45: 80−85.
[38] MARIANI M, GONCHAROV I, MARIANI D, DE G G P, POPOVICH A, LECIS N, VEDANI M. Mechanical and microstructural characterization of WC−Co consolidated by binder jetting additive manufacturing [J]. International Journal of Refractory Metals and Hard Materials, 2021, 100: 105639.
[39] CARREÑO-MORELLI E, ALVEEN P, MOSELEY S, RODRIGUEZ-ARBAIZAR M, CARDOSO K. A comparative study of cemented carbide parts produced by solvent on granules 3D-printing (SG-3DP) versus press and sinter [J]. International Journal of Refractory Metals and Hard Materials, 2021, 97: 105515.
[40] ZHANG Xin-yue, GUO Zhi-meng, CHEN Cun-guang, YANG Wei-wei. Additive manufacturing of WC−20Co components by 3D gel-printing [J]. International Journal of Refractory Metals and Hard Materials, 2018, 70: 215−223.

生坯温等静压提高挤出增材制造 WC−9Co 硬质合金的力学性能

陈 才[1]，周润星[1]，刘祖铭[1]，李咏侠[1,2]，邹 丹[2]，常逸鸣[2]，程许林[2]

1. 中南大学 粉末冶金国家重点实验室，长沙 410083；
2. 湖南博云东方粉末冶金有限公司，长沙 410205

摘 要：针对材料挤出增材制造硬质合金易产生生坯缺陷问题，提出对材料挤出 WC−9Co 硬质合金生坯进行温等静压，以减少或消除生坯缺陷，进而提高其烧结体的组织均匀性和力学性能。生坯温等静压可改善材料挤出硬质合金生坯的缺陷，进而减少烧结样品中的孔隙尺寸和数量，改变烧结体中孔隙形状，同时较好地保持其表面质量和形状特征。与材料挤出−脱脂烧结 WC−9Co 样品相比，采用材料挤出−温等静压−脱脂烧结制备的 WC−9Co 硬质合金的硬度基本保持不变，为 HV_{30} 1494−1508；横向断裂强度最高可提高 49.3%，达到 2998−3514 MPa；断裂韧性保持在较高水平，为 14.8−17.0 MPa·$m^{1/2}$，其综合力学性能明显高于其他增材制造硬质合金，与粉末冶金硬质合金力学性能相当。在材料挤出增材制造技术中引入生坯温等静压，可有效拓宽材料挤出加工窗口，显著提高材料增材制造 WC−Co 硬质合金综合力学性能。

关键词：材料挤出增材制造；WC−Co 硬质合金；温等静压；缺陷；显微组织；力学性能

(Edited by Bing YANG)